Icarus 236 (2014) 83–91

Contents lists available at ScienceDirect

Icarus

journal homepage: www.elsevier.com/locate/icarus

# Chemical composition of Titan's atmosphere and ionosphere: Observations and the photochemical model

Vladimir A. Krasnopolsky *

*Department of Physics, Catholic University of America, Washington, DC 20064, USA*
*Moscow Institute of Physics and Technology, Dolgoprudny, Russia*

ARTICLE INFO

*Article history:*
Received 1 February 2014
Revised 23 March 2014
Accepted 25 March 2014
Available online 8 April 2014

*Keywords:*
Titan, atmosphere
Photochemistry
Atmospheres, composition
Atmospheres, chemistry
Ionospheres

ABSTRACT

Basic observational data on hydrocarbons, nitriles, and ions on Titan are compared with predictions of the photochemical model. Uncertainties of the observed abundances and differences between the data from different instruments and observing teams are comparable with the differences between the observations and the model results. Main reactions of production and loss for each species are quantitatively assessed and briefly discussed. Formation of haze by polymerization of hydrocarbons and nitriles and recombination of heavy ions is calculated along with condensation of various species near the tropopause. Overall deposition is a layer of 300 m thick for the age of the Solar System, and nitrogen constitutes 8% of the deposition. The model reproduces the basic observational data and adequately describes basic chemical processes in Titan's atmosphere and ionosphere. The presented model results and the observational data may be used as a reference to chemical composition of Titan's atmosphere and ionosphere.



## 1. Introduction

Photochemical modeling of Titan's atmosphere is a challenging task, and post-Voyager but pre-Cassini models were developed by Yung et al. (1984), Toublanc et al. (1995), Lara et al. (1996), Banaszkiewicz et al. (2000), and Wilson and Atreya (2004). (Here we do not mention partial models that consider a class of species in adopted background atmosphere.) The first three models did not involve the ion chemistry; Lara et al. (1996) and Banaszkiewicz et al. (2000) neglected effects of the nitrile chemistry on hydrocarbons and vertical transport on some species. However, all these models resulted in gradual progress in the problem. Wilson and Atreya (2004) created the first self-consistent (that is, without adopted background atmosphere) model for coupled neutral and ion chemistry on Titan.

Models by Lavvas et al. (2008) and Hebrard et al. (2007, 2013) were made after the beginning of the Cassini observations. These models do not include ion chemistry that significantly affects some neutral species observed near 1000 km by the ion and neutral mass spectrometer (INMS). Ion chemistry becomes also essential in the lower stratosphere near 100 km. The solar EUV and UV radiation does not reach this region, and the cosmic rays drive photochemistry here. Hebrard et al. (2007) is the most complete of ten papers published on their model. They studied in detail effects of uncertainties in reaction rate coefficients on the species abundances. The calculated uncertainties vary from a few percent to a factor of 40. However, there is no direct correlation between the model uncertainties and differences between the model and observed abundances.

Our self-consistent photochemical model for Titan's atmosphere and ionosphere (Krasnopolsky, 2009, 2010, 2012; henceforth Kr09, Kr10, Kr12) is used for various aspects of Titan's chemical composition. The hydrocarbon and nitrile chemistry of Titan may involve huge numbers of neutral and ion species and their reactions, and our model was aimed to reduce these species and reactions to those that are essential in Titan's chemistry. Finally we use 420 reactions of 83 neutrals and 33 ions, and the adopted reaction rate coefficients may be found in Kr09. Absorption of the solar UV and EUV photons was calculated interactively for the atmospheric gases and by radiative transfer using the aerosol observations from the Huygens probe. Other initial data of the model are the temperature and eddy diffusion profiles (Fig. 1a) and the $N_2$ and $CH_4$ densities at the surface. The model accounts for magnetospheric electrons, protons, and oxygen ions, meteorite influx of $H_2O$, and cosmic rays as well as vertical transport by eddy, molecular, and ambipolar diffusion.

* Address: Department of Physics, Catholic University of America, Washington, DC 20064, USA.
*E-mail address:* vlad.krasn@verizon.net

http://dx.doi.org/10.1016/j.icarus.2014.03.041
0019-1035/

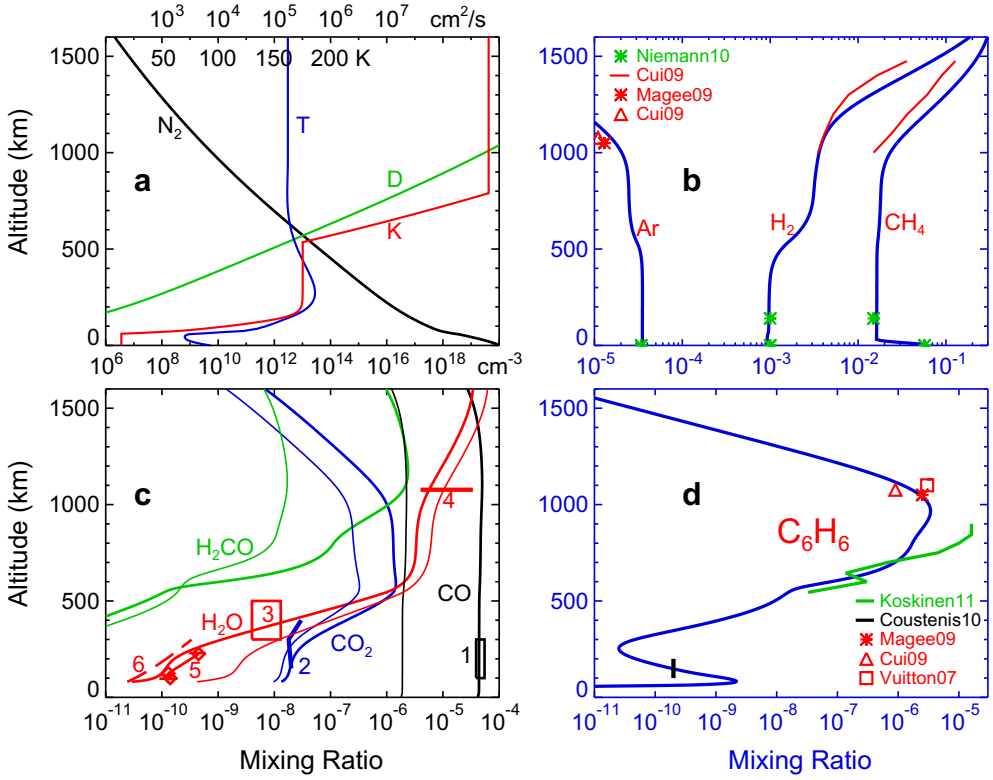


**Fig. 1.** Panel a: temperature, eddy and molecular ($CH_4$ in $N_2$) diffusion profiles (initial data of the model) and the calculated $N_2$. Panel b: basic species. Panel c: oxygen species (from Kr12). Observations: (1) De Kok et al. (2007), (2) Vinatier et al. (2010), (3) Coustenis et al. (1998), (4) Cui et al. (2009), (5) Cottini et al., 2012), (6) Moreno et al. (2012). The model without flux of $O^+$ is shown by thin lines. Panel d: observed and calculated benzene.

There are two versions of the model with hydrodynamic escape of light (less than 20 atomic mass units) species in Kr09 and two versions without hydrodynamic escape (Kr10 and Kr12); thermal escape and escape of ions by the rotating magnetosphere of Saturn remain in these versions. Eddy diffusion was adjusted to provide the best fit to the observational data in the latest version Kr12. Its profile given by six parameters was the only means to improve agreement with the observations. Detailed comparison with the observations was not made in Kr12, while this comparison is important for our understanding of Titan's chemistry. This is a goal of this paper.

The Cassini operations cover currently almost a decade and make it possible to study seasonal variations in the 30-years annual cycle of Titan (Bampasidis et al., 2012; Coustenis et al., 2013). However, our model is aimed at reproduction of the global-mean conditions that are applicable to low and middle latitudes. (All photolysis rates are calculated for the solar zenith angle of 60°, and the sunlight is reduced by a factor of 2 to account for the night side.) Therefore our model is not the best tool to study variations in Titan's atmosphere.

## 2. Observations

Here we will consider observational data that can be directly compared with our model. The ion and neutral mass spectrometer (INMS) provides in situ measurements of the neutral and ion composition above 900 km. However, sampling of the atmosphere and interactions between the sampled species and between those and the instrument are complicated and require modeling in the laboratory. This work was done by two independent teams, and summaries of their results are presented by Magee et al. (2009) and Cui et al. (2009).

Detailed study of the nighttime ion composition at 1100 km during a strong precipitation event T5 was made by Vuitton et al. (2007). The observed ion composition was simulated by a model for this altitude that involved 1250 reactions of 150 ions. Numerous densities of neutral species were parameters of the model, and their best-fit values may be considered as indirect data on the chemical composition at 1100 km.

The ion composition in the T5 encounter was also calculated by Cravens et al. (2009) and in our models. Ionospheric INMS observations from the dayside encounters (Westlake et al., 2012; Mandt et al., 2012) show sums of positive ions that are smaller than electron densities observed simultaneously by the Langmuir probe at RPWS (radio and plasma wave science) and properly extrapolated from the radio occultation observations (Kliore et al., 2008, 2011).

A region of 450–1000 km is covered by stellar occultations (Koskinen et al., 2011) using the ultraviolet imaging spectrometer (UVIS). However, Titan's mesospheric composition is very complicated and includes species whose UV absorption spectra are unknown, while spectra of some other species have not been measured at low temperatures and pressures. This incompleteness of the laboratory data restricts the quality of the UVIS retrievals.

The altitudes below 500 km are probed by limb observations using the composite infrared spectrometer (CIRS). These observations were analyzed by Vinatier et al. (2010) and Nixon et al. (2013), Kutepov et al. (2013) argued that non-LTE effects may affect the retrievals. CIRS nadir observations (Coustenis et al., 2010) refer to altitudes of 100–200 km. There are a few publications on analysis of the CIRS observations; we will use the latest results for low latitudes.

Some data from the IRAM telescope for the millimeter range (Bezard et al., 1993; Marten et al., 2002), the Infrared Space Observatory (ISO, Coustenis et al., 1998), and the Hershel Submillimeter

Observatory (Moreno et al., 2012; Teanby et al., 2013; Rengel et al., 2014) will also be used for comparison with the model.

## 3. Comparison of the observational and model results

Profiles of temperature $T(z)$ and eddy diffusion $K(z)$ are the initial data of the model, and they are shown in Fig. 1a along with a profile of molecular diffusion of $CH_4$ in $N_2$ and a profile of $N_2$ density that is simply calculated using $T(z)$ and the density near the surface. They are discussed in Kr12. All reactions and their rate coefficients with references may be found in Kr09 with minor additions in Kr12.

### 3.1. Argon

Argon is an inert species that is expected to be uniformly mixed below a homopause and depleted as a heavy species above the homopause. However, except the homopause at 1000 km, eddy and molecular diffusions are very similar near 550 km in our model (Fig. 1a). This makes a perturbation and depletion in the Ar profile at 500–600 km (Fig. 1b).

### 3.2. Methane

Methane is saturated in the troposphere and then mixed up to the homopause. Chemical production of methane is weaker than its chemical loss by an order of magnitude (Table 1), and the difference of 7 kg cm$^{-2}$ Byr$^{-1}$ is supplied from the surface. Reaction

$$C_4H_3 + CH_3 \rightarrow C_4H_2 + CH_4$$

provides two-thirds of the methane production. Photolysis is 27% of the methane loss, and the photolysis products CH and metastable $^1CH_2$ react with $CH_4$ and double its loss (21% and 6%, respectively). Photolyses of acetylene and diacetylene result in removal of methane as well:

$$C_2H_2 + h\nu \rightarrow C_2H + H$$
$$C_2 + H_2$$
$$C_4H_2 + h\nu \rightarrow C_2H_2 + C_2$$
$$CH_4 + C_2H \rightarrow C_2H_2 + CH_3 \ (17\%)$$
$$CH_4 + C_2 \rightarrow C_3H_3 + H \ (7\%)$$

Comparing the INMS observations of $CH_4$ and $N_2$ in the upper atmosphere with the Huygens GCMS measurements (Niemann et al., 2010) in the lower atmosphere, Yelle et al. (2006) concluded that either methane is escaping hydrodynamically with the diffusion-limited flow of $3.5 \times 10^9$ cm$^{-2}$ s$^{-1}$ or eddy diffusion is extremely strong in the upper atmosphere with $K = (4 \pm 3) \times 10^9$ cm$^2$ s$^{-1}$. Yelle et al. (2008) and Cui et al. (2012) involved the observed Ar in their analyses and concluded that $K \approx 2 \times 10^7$ cm$^2$ s$^{-1}$ and methane is escaping with a rate that is close to the diffusion limit. There are some arguments pro and contra the hydrodynamic escape of methane (see e.g. Kr10, Cui et al. (2012)), and our model applies a moderate $K = 6.5 \times 10^8$ cm$^2$ s$^{-1}$ (Fig. 1a) without hydrodynamic escape. That is why Ar and $CH_4$ in our model (Fig. 1b) are slightly larger and smaller in the upper atmosphere than those observed (by factors of 1.3 and 1.6, respectively).

### 3.3. Molecular hydrogen

Unlike Ar and $CH_4$, $H_2$ and all other photochemical products are not fixed at the surface in the model. The calculated profile (Fig. 1b) just coincides with the observed GCMS values and the INMS data at 1000–1200 km. The calculated abundances are larger than those observed at 1500 km by a factor 1.7, and this difference could be removed by increasing of eddy diffusion. However, this increase is not favorable for other species.

Sixty-five reactions produce $H_2$ in our model. Both $H_2$ and H are formed by photolyses of hydrocarbons, and the H—H bond is stronger than H—C bonds in hydrocarbons. Therefore most of the H atoms recombine finally to $H_2$. Chemical loss of $H_2$ is smaller than its production by two orders of magnitude (Table 1), and almost all $H_2$ molecules escape.

The second homopause at 550 km in our model results in an enrichment in $H_2$ above 650 km by a factor of 3. Thermal escape of $H_2$ is equal to $1.15 \times 10^{10}$ cm$^{-2}$ s$^{-1}$ (Table 1) and may be compared with the diffusion limit $bf/H$. Here $b = n\ D_{H2} = 1.88 \times 10^{17}\ T^{0.82}$ cm$^{-1}$ s$^{-1}$ (Chamberlain and Hunten, 1987), $D_{H2}$ is the diffusion coefficient of $H_2$ in $N_2$, $f$ is the $H_2$ mixing ratio below the homopause at 1000 km, $n$ and $H$ are the atmospheric number density and scale height. Substituting all values with the proper reduction to the surface, we conclude that the calculated thermal escape of $H_2$ is diffusion-limited in our model.

### 3.4. Ethane $C_2H_6$

The single C—C bonds are formed mainly by reaction

$$CH_3 + CH_3 + M \rightarrow C_2H_6 + M$$

that is almost completely responsible for the production of ethane in our model (Fig. 2c), while the contribution of the other reactions is less than 1%. Condensation of ethane consumes two thirds of its production (Table 1), and a third is removed in reactions with various radicals. Photolysis of ethane is significantly depleted by absorption of methane and therefore weak.

Early analyses of the CIRS limb observations favored a constant ethane mixing ratio of ~15 ppm from 150 to 400 km (see Vinatier et al. (2010) and references therein). The recent results by Nixon et al. (2013) extend from 125 to 225 km with a maximum at

**Table 1**
Column production and loss rates, escape/precipitation flows, and mean chemical lifetimes of some species.

| Species | H | $H_2$ | $CH_4$ | $C_2H_2$ | $C_2H_4$ | $C_2H_6$ | $C_3H_4$ | $C_3H_6$ | $C_3H_8$ |
|---|---|---|---|---|---|---|---|---|---|
| Production (cm$^{-2}$ s$^{-1}$) | 1.55 + 10 | 1.17 + 10 | 1.13 + 9 | 5.83 + 9 | 2.66 + 9 | 1.54 + 9 | 4.97 + 8 | 2.51 + 8 | 2.29 + 8 |
| Loss (cm$^{-2}$ s$^{-1}$) | 1.36 + 10 | 1.94 + 8 | 9.60 + 9 | 5.67 + 9 | 2.66 + 9 | 5.17 + 8 | 4.97 + 8 | 2.51 + 8 | 5.02 + 7 |
| Flow (g cm$^{-2}$ Byr$^{-1}$) | 101 | 1210 | 7132 | −212 | – | −1610 | – | – | −415 |
| Lifetime (yr) | 0.003 | 5.95 + 5 | 2.85 + 7 | 17.5 | 0.61 | 562 | 0.44 | 0.72 | 264 |
| | $C_4H_2$ | $C_6H_6$ | HCN | $HC_3N$ | $CH_3CN$ | $C_2N_2$ | $H_2O$ | CO | $CO_2$ |
| Production (cm$^{-2}$ s$^{-1}$) | 5.60 + 9 | 2.15 + 8 | 1.20 + 9 | 1.59 + 9 | 1.58 + 7 | 6.17 + 6 | 5.71 + 6 | 4.35 + 6 | 4.35 + 6 |
| Loss (cm$^{-2}$ s$^{-1}$) | 5.60 + 9 | 1.92 + 8 | 1.05 + 9 | 1.52 + 9 | 7.88 + 6 | 4.22 + 6 | 1.04 + 7 | 4.35 + 6 | 2.56 + 6 |
| Flow (g cm$^{-2}$ Byr$^{-1}$) | – | −9.44 | −207 | −169 | −17.4 | −5.3 | – | – | −4.1 |
| Lifetime (yr) | 0.03 | 0.73 | 13.2 | 2.66 | 27.7 | 53.7 | 2.18 | 7.57 + 7 | 443 |

Positive flows are escape or sublimation from the surface, negative flows are condensation; precipitation of haze is not given (see section 3.18); all values are reduced to the surface; 1.55 + 10 = $1.55 \times 10^{10}$.

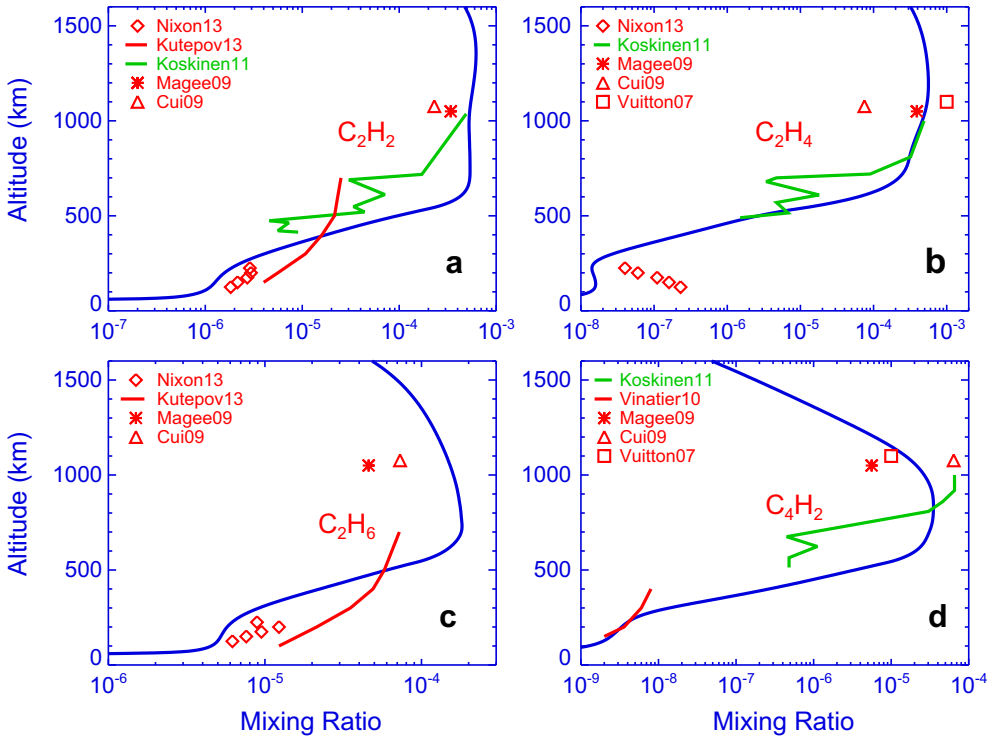


**Fig. 2.** Calculated and observed abundances of $C_2H_X$ hydrocarbons and $C_4H_2$.

200 km (Fig. 2c), and the mean difference between these data and the model is a factor of 1.6. A preliminary attempt to account for non-LTE effects in the CIRS limb data (Kutepov et al., 2013) is shown as well. The $C_2H_6$ abundance at 1000–1100 km in the model exceeds those from the INMS observations by a factor of 2.5.

### 3.5. Ethylene $C_2H_4$

Formation of the C=C double bonds occurs mostly via

$$CH_4 + CH \rightarrow C_2H_4 + H$$

that contributes three quarters of the ethylene production (Table 1), while the photolysis is responsible for three quarters of the loss. Some part of $CH_2$ and $CH_3$ formed by photolysis of $CH_4$ is converted to CH in reactions with H, and an effective yield of $C_2H_4$ in photolysis of $CH_4$ is 0.77, so that the effective quantum loss of $CH_4$ is 1.77.

Production and loss of $C_2H_4$ proceed mostly at 600–1000 km, and our model agrees with the INMS data from three teams (Fig. 2b) and even with the UVIS occultations. Ethylene does not condense in our model, and the secondary peak at 150 km is caused by the steep increase in eddy diffusion (Fig. 1a) and chemistry initiated by the cosmic rays. A mean difference between the model and the recently published CIRS observations at 125–225 km (Nixon et al., 2013) is a factor of 6.

### 3.6. Acetylene $C_2H_2$

Acetylene (Table 1, Fig. 2a) is formed by photolysis of $C_2H_4$ (35%) and some other hydrocarbons (17%), $C_2H + CH_4$ (28%), and other reactions of radicals. The most significant loss is by photolysis (42% of the production) and in

$$C_2H_2 + C_2H \rightarrow C_4H_2 + H \ (16\%)$$
$$C_2H_2 + CN \rightarrow HC_3N + H \ (16\%)$$

that form diacetylene and cyanoacetylene, respectively. Condensation removes 3% of the $C_2H_2$ production.

The calculated profile of $C_2H_2$ agrees with the recent CIRS results and the INMS data with mean differences of factors of 1.6 and 1.8, respectively. The UVIS occultation and a preliminary non-LTE CIRS profile are also shown for comparison.

### 3.7. Propyne $C_3H_4$

Our model does not separate propyne $CH_3C_2H$ and allene $CH_2CCH_2$; yields of propyne are typically larger than those of allene, and allene has not been detected on Titan. The calculated profile of propyne is shown in Fig. 3a. Production of propyne is mostly by reactions

$$C_3H_3 + H + M \rightarrow C_3H_4 + M \ (86\%, 302 \text{ km})$$
$$C_2H_4 + CH \rightarrow C_3H_4 + H \ (6\%, 820 \text{ km})$$
$$C_3H_5 + H \rightarrow C_3H_4 + H_2 \ (5\%, 485 \text{ km})$$

Propyne is lost in

$$C_3H_4 + H \rightarrow C_2H_2 + CH_3 \ (89\%, 345 \text{ km})$$

and by photolysis (9%, 300 km). Condensation of propyne is insignificant. The weighted-mean altitudes of the reactions given in parentheses indicate that the basic $C_3H_4$ chemistry proceeds near 300 km. However, the propyne mixing ratio peaks at 1050 km and exceeds that near 300 km by two orders of magnitude. This is due to dissociative recombination of $C_4H_5^+$ that contributes just 0.4% but in the low-density upper atmosphere.

The calculated profile agrees with the CIRS data (within a factor of 1.6) and the INMS value (within a factor of 2).

### 3.8. Propylene $C_3H_6$

Propylene was recently detected in Titan's stratosphere by averaging of numerous CIRS limb spectra (Nixon et al., 2013). The profile from our model (Kr12) along with the CIRS and INMS data are shown in Fig. 4, and the agreement of the model prediction with the observations is excellent.

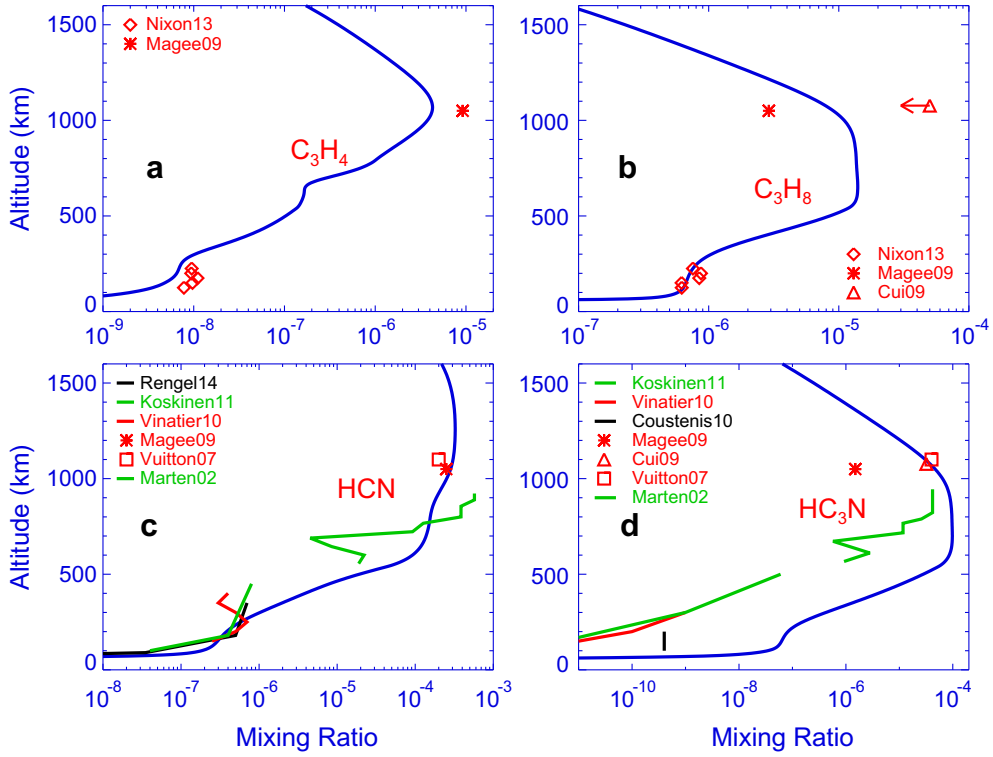


**Fig. 3.** Calculated profiles and observational data of propyne, propane, hydrogen cyanide, and cyanoacetylene.

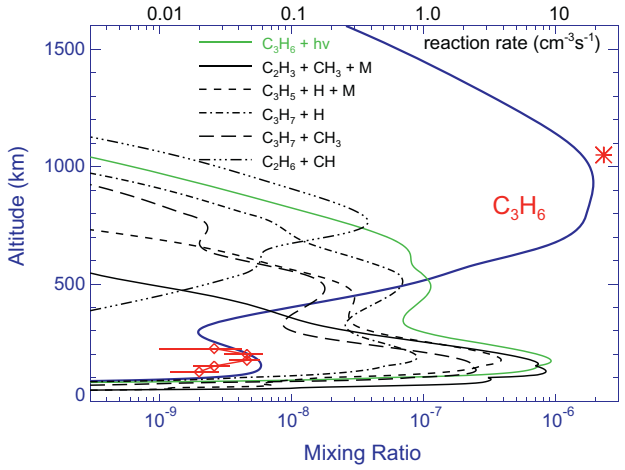


**Fig. 4.** Vertical profile of propylene in our model is compared with the CIRS (Nixon et al., 2013, small diamonds) and INMS (Magee et al., 2009, asterisk) detections. Profiles of the propylene removal by photolysis and production in five processes are shown as well.

Chemistry of propylene involves 23 reactions in our model. Profiles of five main reactions are shown in Fig. 4. Photolysis constitutes two thirds of the loss, and the other third is the two- and three-body reactions with H, both are effective near 150 km. The most significant production by $C_2H_3 + CH_3 + M \rightarrow C_3H_6 + M$ (42%) peaks near 150 km as well. Three other production reactions

$$C_3H_5 + H + M \rightarrow C_3H_6 + M \ (22\%)$$
$$C_3H_7 + H \rightarrow C_3H_6 + H_2 \ (15\%)$$
$$C_3H_7 + CH_3 \rightarrow C_3H_6 + CH_4 \ (14\%)$$

have secondary peaks near 500 km (Fig. 4). Another reaction

$$C_2H_6 + CH \rightarrow C_3H_6 + H \ (5\%)$$

peaks at 800 km, where the atmospheric density is low, and results in a propylene mixing ratio of ~1.5 ppm at 700–1000 km.

Chemistry near 150 km is a balance between the effects of cosmic rays and condensation processes that strongly deplete almost all species. Chemistry near 500 km is initiated by photolyses of photochemical products. The predicted peak in the $C_3H_6$ mixing ratio near 150 km is well reproduced by the CIRS observations. The model agrees with the INMS measurement of propylene as well.

### 3.9. Propane $C_3H_8$

Propane (Fig. 3b, Table 1) is formed by the reaction between ethyl and methyl radicals:

$$C_2H_5 + CH_3 + M \rightarrow C_3H_8 + M \ (97\%, 306 \text{ km})$$

78% of the propane production condenses, and the remaining propane is removed by photolysis (3%) and in reactions with the $C_2$, $C_2H$, and $C_4H$ radicals (2.5%, 15%, and 1.6%, respectively).

The model profile of propane is in excellent agreement with the recent CIRS data (Nixon et al., 2013) in the stratosphere and between the INMS values from two teams in the thermosphere.

### 3.10. Diacetylene $C_4H_2$

The production and loss rates of $C_4H_2$ in Table 1 are corrected for the excitation and quenching without chemical reaction of the metastable state of this species. The following processes dominate in the production of diacetylene:

$$C_4H_3 + H \rightarrow C_4H_2 + H_2 (49\%)$$

$$C_4H_4 + h\nu \rightarrow C_4H_2 + H_2 \ (21\%)$$

$$C_2H_2 + C_2H \rightarrow C_4H_2 + H \ (16\%)$$

$$C_4H_3 + CH_3 \rightarrow C_4H_2 + CH_4 \ (13\%)$$

Diacetylene is lost in radiative and three-body association with H, photolysis, and haze formation:

$C_4H_2 + H \rightarrow C_4H_3 + h\nu$ (79%)

$C_4H_2 + H + M \rightarrow C_4H_3 + M$ (4%)

$C_4H_2 + h\nu \rightarrow C_4H, C_2H_2, C_2, H$ (7%)

$C_4H_2 + C_3N \rightarrow$ polymer (5%)

$C_4H_2 + C_6H \rightarrow$ polymer (3%)

The $C_4H_2$ abundance is small below 150 km, and its condensation is insignificant. The model profile of diacetylene (Fig. 2d) agrees with the CIRS data below 300 km and just in the middle of the INMS values.

### 3.11. Benzene $C_6H_6$

Column production of benzene is $2.15 \times 10^8$ cm$^{-2}$ s$^{-1}$ (Table 1, Fig. 1d); it includes formation of the $C_6$ rings in

$C_4H_5 + C_2H_2 \rightarrow C_6H_6 + H$ (23%, 82 km)

$C_3H_3 + C_3H_3 + M \rightarrow C_6H_6 + M$ (4%, 346 km)

recycling in

$C_6H_5 + H \rightarrow C_6H_6 + h\nu$ (64%, 461 km)

and dissociative recombination of $C_6H_7^+$ and $C_7H_7^+$ (8%, 860 km). Weighted-mean altitudes of these reactions are given in parentheses. The bulk production of the $C_6$ rings and a sharp peak in the benzene mixing ratio (Fig. 1d) are at the very low altitudes and initiated by the cosmic rays. The production by the ion chemistry results in a steep increase in the benzene mixing ratio to 1000 km by a few orders of magnitude.

Loss of benzene is by photolysis and condensation (89% and 11%, respectively). The model profile agrees with the CIRS nadir, INMS, and UVIS observations.

### 3.12. Hydrogen cyanide HCN

$N_2$ is a very tough molecule, and atomic nitrogen is formed by predissociation, electron impact dissociation, and dissociative ionization of $N_2$ with a column rate of $6.3 \times 10^8$ cm$^{-2}$ s$^{-1}$. Nitrogen atoms may react with hydrocarbon radicals and form nitriles $C_XH_YCN$. The C≡N triple bond is strong with energy ~8 eV and cannot be destroyed in Titan's atmosphere. Therefore all nitriles precipitate to the surface after some mutual conversions, and the precipitation rate of N is 460 g cm$^{-2}$ Byr$^{-1}$. Reaction of $N + CH_3 \rightarrow H_2CN + H$ is the main source of nitriles on Titan that consumes a half of the atomic nitrogen production.

HCN (Table 1, Fig. 3c) is formed by reactions:

$H_2CN + H \rightarrow HCN + H_2$ (24%, 920 km)

$CN + CH_4 \rightarrow HCN + CH_3$ (39%, 183 km)

$CN + C_2H_4 \rightarrow HCN + C_2H_3$ (11%, 750 km)

$CN + C_2H_6 \rightarrow HCN + C_2H_5$ (6%, 350 km)

HCN is lost in reactions:

$C_2H_3 + HCN \rightarrow C_2H_3CN + H$ (32%, 122 km)

$C_3N + HCN \rightarrow C_4N_2 + H$ (27%, 618 km)

$CH + HCN \rightarrow CHCN + H$ (9%, 807 km)

$HCN + h\nu \rightarrow CN + H$ (6%, 739 km)

Ion reactions add and remove 19% and 14%, respectively, and condensation removes 12% of the total production. The weighted-mean altitudes indicate that the strongest reactions of $CN + CH_4$ and $C_2H_3 + HCN$ are effective in the lower stratosphere and almost balance each other. The model profile agrees with the observations (Fig. 3c).

### 3.13. Cyanoacetylene $HC_3N$

$HC_3N$ is another abundant nitrile on Titan (Table 1, Fig. 3d). It is produced by

$CN + C_2H_2 \rightarrow HC_3N + H$ (60%, 541 km)

$C_3N + CH_4 \rightarrow HC_3N + CH_3$ (40%, 371 km)

The removal is by photolysis (86%), condensation (4%), polymerization (1%), reactions with $C_2H$ and CN (1.5%), and reactions with $HCNH^+$ and $C_2H_5^+$ (8%).

There is a significant difference between the $HC_3N$ abundances retrieved from the INMS neutral spectra by Magee et al. (2009) and Cui et al. (2009). The latter agrees with that from the INMS ion spectra (Vuitton et al., 2007), UVIS, and our model (Fig. 3d). $HC_3N$ in the stratosphere from our model significantly exceeds the CIRS data.

Clarke and Ferris (1996) found that irradiation at 185–254 nm results in intense polymerization in pure $HC_3N$ and when mixed in $CH_4$, $C_2H_2$, and CO. However, no kinetic data were deduced from their study, and basic polymerization reactions related to $HC_3N$ in our model are (Lavvas et al., 2008)

$HC_3N + C_4H \rightarrow$ polymer

$C_3N + C_4H_2 \rightarrow$ polymer

It looks like the loss to polymerization is underestimated in our model, and a greater loss could reduce the $HC_3N$ abundances in the stratosphere to the observed values.

### 3.14. Cyanogen $C_2N_2$

Cyanogen (Table 1, Fig. 5) is formed by reactions

$CN + CH_2CN \rightarrow C_2N_2 + CH_2$ (85%, 660 km)

$N + CHCN \rightarrow C_2N_2 + H$ (15%, 246 km)

The loss is by photolysis and condensation (68% and 32%, respectively). The model profile agrees with the INMS value by Magee

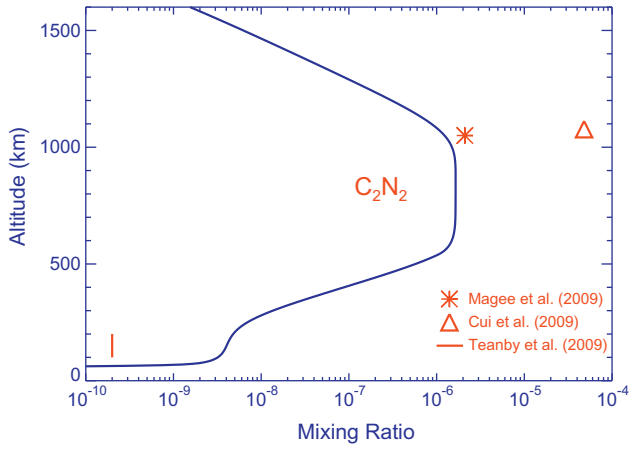


**Fig. 5.** Vertical profile and observations of cyanogen.

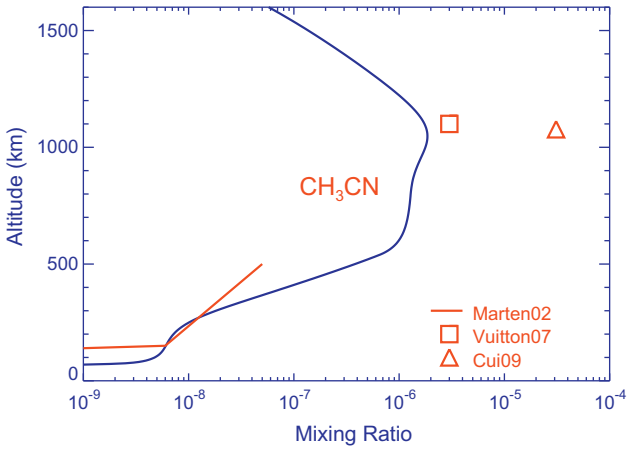


**Fig. 6.** Observations and model of acetonitrile.

et al. (2009) but significantly exceeds the CIRS observations. This may be explained by polymerization of $C_2N_2$, which is very weak in our model and may be underestimated.

### 3.15. Acetonitrile $CH_3CN$

$CH_3CN$ was detected on Titan in the millimeter range using the IRAM telescope by Bezard et al. (1993). Later results from the same telescope by Marten et al. (2002) are shown in Fig. 6 along with the INMS retrievals by Vuitton et al. (2007) and Cui et al. (2009). The model profile is in reasonable agreement with the ground-based data and Vuitton et al. (2007).

$CH_3CN$ is formed by

$$CH_2CN + H + M \rightarrow CH_3CN + M \ (53\%, 142 \text{ km})$$

$$N(^2D) + C_2H_4 \rightarrow CH_3CN + H \ (25\%, 981 \text{ km})$$

$$N + C_2H_3 + M \rightarrow CH_3CN + M \ (20\%, 62 \text{ km})$$

Condensation dominates in the loss of $CH_3CN$ (50%), and other losses are by ion reactions and photolysis:

$$HCNH^+ + CH_3CN \rightarrow CH_3CNH^+ + HCN \ (29\%, 370 \text{ km})$$

$$C_2H_5^+ + CH_3CN \rightarrow CH_3CNH^+ + C_2H_4 \ (14\%, 515 \text{ km})$$

$$CH_3CN + h\nu \rightarrow CH_3 + CN \ (6\%, 503 \text{ km})$$

The above ion reactions have peaks near 80 and 1000 km, and the weighted-mean altitudes reflect proportions of these peaks.

### 3.16. Some other neutral species

Oxygen chemistry in our model was considered in detail in Kr12, and Fig. 1c is reproduced from that paper. The model is in excellent agreement with the observed abundances of CO, $H_2O$, and $CO_2$. Influxes of meteoritic water and magnetospheric $O^+$ are the sources of the oxygen species on Titan.

The model profiles of some other neutral species may be found in Kr12. Some of them were detected by INMS in the neutral mode (Magee et al., 2009; Cui et al., 2009) and retrieved from the ion spectra (Vuitton et al., 2007). These data are collected and compared with the model in Table 2.

The most significant differences between the model and observed values are for ammonia $NH_3$, $C_7H_4$, and $C_7H_8$. Recent observations using the Hershel Submillimeter Observatory established an upper limit of $1.23 \times 10^{15}$ cm$^{-2}$ to the column abundance of ammonia (Teanby et al., 2013); our model predicted $1.4 \times 10^{15}$ cm$^{-2}$. The differences between the observed values for these species are large as well. Overall, the differences between the model and observed values in Table 2 are comparable to the differences between the abundances retrieved by the three teams.

### 3.17. Ions

Vertical profiles of the most abundant ions in Titan's ionosphere are shown in Kr12 for the mean conditions and for the night time during a strong precipitation of magnetospheric electrons (T5 encounter). The model involves ambipolar diffusion and escape of ions at half diffusion velocity. It was mentioned in Section 2 that sums of positive ions observed by INMS on the day side are smaller than electron densities measured simultaneously by the Langmuir probe of RPWS and those properly extrapolated from the radio occultations (Kliore et al., 2008, 2011). The observed ion composition at ~1100 km during the T5 encounter (Vuitton et al., 2007; Cravens et al., 2009) is therefore better suited for analysis and compared in Table 3 with results of three models.

To make a quantitative assessment to fitting of observations by models, we suggested a difference factor that is equal to a mean ratio of observed-to-model values or vise versa so that the biggest value is always in the numerator (Kr09, Kr12). This factor is 2.42 for our model, while it is 1.74 for Vuitton et al. (2007), who calculated the ion composition at 1100 km using 1250 reactions of 150 ions with densities of 18 neutral species as fitting parameters. Our model involves 111 reactions of 33 ions, because of our general intent to remove species and reactions of minor importance, and does not include fitting parameters. Comparing the results, one may conclude that the model adequately describes the ionospheric chemistry on Titan.

### 3.18. Haze

Haze is formed on Titan by polymerization and condensation of hydrocarbons and nitriles and recombination of heavy ions. Condensation rates for photochemical products are given in Table 1; haze production by polymerization and recombination is shown in Fig. 7.

Polymerization of $C_4H_2$ in reactions with $C_6H$ and $C_3N$ produce 75% and 95% of hydrocarbon and nitrile polymers. Both processes peak near 570 km, and polymerization of nitriles becomes significant at 1000 km. Recombination of heavy ions is another source of haze. The heaviest ions in our model are $C_{10}H_{11}^+$, $C_{10}H_9^+$, and $C_9H_{11}^+$ with masses of 131, 129, and 119 amu, and their recombination

**Table 2**
Mixing ratios of some species retrieved from the INMS observations and in our model.

| Reference | $h$ (km) | $C_6H_2$ | $C_7H_4$ | $C_7H_8$ | $NH_3$ | $CH_2NH$ | $C_2H_3CN$ | $C_2H_5CN$ | $C_4H_3N$ | $HC_5N$ | $C_5H_5N$ |
|---|---|---|---|---|---|---|---|---|---|---|---|
| Magee et al. (2009) | 1050 | – | – | 2.5–8 | – | – | 3.5–7 | 1.5–7 | – | – | – |
| Cui et al. (2009) | 1077 | – | – | <1.3–7 | 3–5 | – | <1.8–5 | – | – | – | – |
| Vuitton et al. (2007) | 1100 | 8–7 | 3–7 | 2–7 | 7–6 | 1–5 | 1–5 | 5–7 | 4–6 | 1–6 | 4–7 |
| This model | 1075 | 2.8–6 | 1.5–9 | 3.8–9 | 1–6 | 1.8–5 | 1.1–5 | 1.5–7 | 4.5–6 | 5–6 | 5–7 |

2.5–8 = $2.5 \times 10^{-8}$.

**Table 3**
Number densities (in $cm^{-3}$) of the most abundant ions in the nighttime ionosphere during a strong precipitation event T5. The INMS data at 1100 km are compared with three models.

| Ion | $HCNH^+$ | $HC_3NH^+$ | $C_3H_3^+$ | $C_2H_3CNH^+$ | $CH_2NH_2^+$ | $C_2H_5^+$ | $C_3H_5^+$ | $CH_3CNH^+$ | $C_5H_5^+$ |
|---|---|---|---|---|---|---|---|---|---|
| INMS | 302 | 97 | 85 | 85 | 58 | 50 | 46 | 45 | 29 |
| VYM | 460 | 140 | 34 | 130 | 48 | 200 | 100 | 73 | 27 |
| Cr09 | 1510 | 2.5 | 9.0 | 26 | 62 | 70 | 39 | 42 | 4.6 |
| This model | 146 | 94 | 8.2 | 24 | 99 | 74 | 81 | 26 | 49 |

| | $C_4H_3^+$ | $C_4H_3NH^+$ | $C_5H_7^+$ | $C_4H_5^+$ | $C_7H_7^+$ | $NH_4^+$ | $C_6H_7^+$ | $CH_3^+$ | $CH_5^+$ | $C_6H_5^+$ | $F$ |
|---|---|---|---|---|---|---|---|---|---|---|---|
| INMS | 27 | 26 | 19 | 17 | 13 | 9.2 | 7.5 | 6.6 | 6.5 | 5.6 | |
| VYM | 34 | 39 | 35 | 16 | 21 | 15 | 14 | 9.5 | 30 | 2.7 | 1.74 |
| Cr09 | 1.5 | 76 | 3.7 | 2.0 | 0.03 | 15 | 2.4 | 9.1 | 58 | 0.07 | 5.83 |
| This model | 61 | 13 | 10.5 | 45 | 39 | 0.5 | 7.4 | 2.7 | 6.9 | 11.7 | 2.42 |

VYM is Vuitton et al. (2007), Cr09 is Cravens et al. (2009), $F$ is the difference factor.

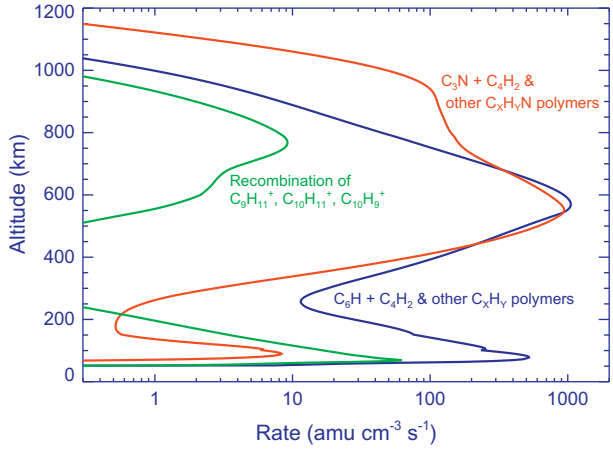


**Fig. 7.** Production of haze on Titan by polymerization of hydrocarbons and nitriles and recombination of heavy ions.

**Table 4**
Precipitation of photochemical products (in g $cm^{-2}$ $Byr^{-1}$).

| | |
|---|---|
| $C_xH_y$ polymerization | 1645 |
| $C_xH_yN$ polymerization | 1650 |
| Recombination of heavy ions | 26 |
| $C_xH_y$ condensation | 2246 |
| $C_xH_yN$ condensation | 400 |
| Total | 5967 |

peaks at 770 km. Strong secondary peaks of all three sources of haze are near 100 km and due to chemistry initiated by the cosmic rays.

Summary of deposition rates to the surface from all photochemical products is given in Table 4. Polymerizations of hydrocarbons and nitriles have equal rates while their condensation rates are very different. The deposition by condensation does not account for possible partial sublimation near the surface, where the atmosphere is warmer than at the tropopause (94 and 70 K, respectively). The total deposition of nitrogen is 460 g $cm^{-2}$ $Byr^{-1}$, that is, 8% of the total deposition rate of 6 kg $cm^{-2}$ $Byr^{-1}$. The model implies a surface deposit thickness of ~300 m for the age of the Solar System, and one may expect that this deposit could be reprocessed and in some part returned into the atmosphere.

## 4. Conclusions

Basic observational data on hydrocarbons, nitriles, and ions on Titan are compared with predictions of the photochemical model. Uncertainties of the observed abundances and differences between the data from different instruments and observing teams are comparable with the differences between the observations and the model results. Main reactions of production and loss for each species are quantitatively assessed and briefly discussed. Formation of haze by polymerization of hydrocarbons and nitriles and recombination of heavy ions is calculated along with condensation of various species near the tropopause. Overall deposition is a layer of 300 m thick for the age of the Solar System, and nitrogen constitutes 8% of the deposition. The model reproduces the basic observational data and adequately describes basic chemical processes in Titan's atmosphere and ionosphere. The presented model results and the observational data may be used as a reference to chemical composition of Titan's atmosphere and ionosphere.

The model file is available by request to Vlad.Krasn@verizon.net.

## Acknowledgment

This work is supported by Grant 11.G34.31.0074 of the Russian Government to Moscow Institute of Physics and Technology (PhysTech) and V.A. Krasnopolsky.

## References

Bampasidis, G. et al., 2012. Thermal and chemical structure variations in Titan's stratosphere during the Cassini mission. Astrophys. J. 760, 144 (8 pp.).
Banaszkiewicz, M., Lara, L.M., Rodrigo, R., Lopez-Moreno, J.J., Molina-Cuberos, G.J., 2000. A coupled model of Titan's atmosphere and ionosphere. Icarus 147, 386–404.
Bezard, B., Marten, A., Paubert, G., 1993. Detection of acetonitrile on Titan. Bull. Am. Astron. Soc. 25, 1100 (abstract).
Chamberlain, J.W., Hunten, D.M., 1987. Theory of Planetary Atmospheres. Academic Press, Orlando.
Clarke, D.W., Ferris, J.P., 1996. Titan haze: Mechanism of cyanoacetylene photochemistry at 185 and 254 nm. J. Geophys. Res. 101, 7575–7584.
Cottini, V. et al., 2012. Water vapor in Titan's stratosphere from Cassini CIRS far-infrared spectra. Icarus 220, 855–862.
Coustenis, A. et al., 1998. Evidence for water vapor in Titan's atmosphere from ISO/SWS data. Astron. Astrophys. 336, L85–L89.
Coustenis, A. et al., 2010. Titan trace gaseous composition from CIRS at the end of the Cassini–Huygens prime mission. Icarus 207, 461–476.
Coustenis, A. et al., 2013. Evolution of the stratospheric temperature and chemical composition over one titanian year. Astrophys. J. 779, 177 (9 pp.).
Cravens, T.E. et al., 2009. Models-data comparison for Titan's nightside ionosphere. Icarus 199, 174–188.
Cui, J. et al., 2009. Analysis of Titan's neutral upper atmosphere from Cassini Ion Neutral Mass Spectrometer measurements. Icarus 200, 581–615.
Cui, J. et al., 2012. The $CH_4$ structure in Titan's upper atmosphere revisited. J. Geophys. Res. 117, E11006.
De Kok, R. et al., 2007. Oxygen compounds in Titan's stratosphere as observed by Cassini CIRS. Icarus 186, 354–363.
Hebrard, E., Dobrijevic, M., Benilan, Y., Raulin, F., 2007. Photochemical kinetics uncertainties in modeling Titan's atmosphere: First consequences. Planet. Space Sci. 55, 1470–1489.
Hebrard, E., Dobrijevic, M., Loison, J.C., Bergeat, A., Hickson, K.M., Caralp, P., 2013. Photochemistry of $C_3H_p$ hydrocarbons in Titan's stratosphere revisited. Astron. Astrophys. 552, A132 (21 pp.).

Kliore, A.J. et al., 2008. First results from the Cassini radio occultations of the Titan ionosphere. J. Geophys. Res. 113, A09317. http://dx.doi.org/10.1029/2007JA012965.

Kliore, A.J., Nagy, A.F., Cravens, T.E., Richard, M.S., Rymer, A.M., 2011. Unusual electron density profiles observed by Cassini radio occultations in Titan's ionosphere: Effects of enhanced magnetospheric electron precipitation? J. Geophys. Res. 116, A11318.

Koskinen, T.T., Yelle, R.V., Snowden, D.S., Lavvas, P., Sandel, B.R., Capalbo, F.J., Benilan, Y., West, R.A., 2011. The mesosphere and thermosphere of Titan revealed by Cassini/UVIS stellar occultations. Icarus 216, 507–534.

Krasnopolsky, V.A., 2009. A photochemical model of Titan's atmosphere and ionosphere. Icarus 201, 226–256.

Krasnopolsky, V.A., 2010. The photochemical model of Titan's atmosphere and ionosphere: A version without hydrodynamic escape. Planet. Space Sci. 58, 1507–1515.

Krasnopolsky, V.A., 2012. Titan's photochemical model: Further update, oxygen species, and comparison with Triton and Pluto. Planet. Space Sci. 73, 318–326.

Kutepov, A., Vinatier, S., Feofilov, A., Nixon, C., Boursier, C., 2013. Non-LTE diagnostics of CIRS observations of the Titan's mesosphere. Am. Astron. Soc., DPS Meeting #45, #207.05.

Lara, L.M., Lellouch, E., Lopes-Moreno, J., Rodrigo, R., 1996. Vertical distribution of Titan's atmospheric neutral constituents. J. Geophys. Res. 101, 23261–23283.

Lavvas, P.P., Coustenis, A., Vardavas, I.M., 2008. Coupling photochemistry with haze formation in Titan's atmosphere, Part II: Results and validation with Cassini/Huygens data. Planet. Space Sci. 56, 67–99.

Magee, B.A., Waite, J.H., Mandt, K.E., Westlake, J., Bell, J., Gell, D.A., 2009. INMS-derived composition of Titan's upper atmosphere: Analysis methods and model comparison. Planet. Space Sci. 57, 1895–1916.

Mandt, K.E. et al., 2012. Ion densities and composition of Titan's upper atmosphere derived from the Cassini Ion Neutral Mass Spectrometer: Analysis methods and comparison of measured ion densities to photochemical model simulations. J. Geophys. Res. 117, E10006.

Marten, A., Hidayat, T., Biraud, Y., Moreno, R., 2002. New millimeter heterodyne observations of Titan: Vertical distributions of nitriles HCN, $HC_3N$, $CH_3CN$, and the isotopic ratio $^{15}N/^{14}N$ in its atmosphere. Icarus 158, 532–544.

Moreno, R., Lellouch, E., Lara, L.M., Feuchtgruber, H., Rengel, M., Hartogh, P., Courtin, R., 2012. The abundance, vertical distribution and origin of $H_2O$ in Titan's atmosphere: Hershel observations and photochemical modeling. Icarus 221, 753–767.

Niemann, H.B. et al., 2010. Composition of Titan's lower atmosphere and simple surface volatiles as measured by the Cassini–Huygens probe gas chromatograph mass spectrometer experiment. J. Geophys. Res. 115, E12006.

Nixon, C.A. et al., 2013. Detection of propylene in Titan's stratosphere. Astrophys. J. 776, L14 (6 pp.).

Rengel, M. et al., 2014. Hershel/PACS spectroscopy of trace gases of the stratosphere of Titan. Astron. Astrophys. 561, A4 (6 pp.).

Teanby, N.A., Irwin, P.G.J., de Kok, R., Jolly, A., Bezard, B., Nixon, C.A., Calcutt, S.B., 2009. Titan's stratospheric $C_2N_2$, $C_3H_4$, and $C_4H_2$ abundances from Cassini/CIRS far-infrared spectra. Icarus 202, 620–631.

Teanby, N.A. et al., 2013. Constraints on Titan's middle atmosphere ammonia abundance from Hershel/SPIRE sub-millimeter spectra. Planet. Space Sci. 75, 136–147.

Toublanc, D., Parisot, J.P., Brillet, J., Gautier, D., Raulin, F., McKay, C.P., 1995. Photochemical modeling of Titan's atmosphere. Icarus 113, 2–26.

Vinatier, S. et al., 2010. Analysis of Cassini/CIRS limb spectra of Titan acquired during the nominal mission. I. Hydrocarbons, nitriles and $CO_2$ vertical mixing ratio profiles. Icarus 205, 559–570.

Vuitton, V., Yelle, R.V., McEwan, M.J., 2007. Ion chemistry and N-containing molecules in Titan's upper atmosphere. Icarus 191, 722–742.

Westlake, J.H. et al., 2012. Titan's ionospheric composition and structure: Photochemical modeling of Cassini INMS data. J. Geophys. Res. 117, E01003.

Wilson, E.H., Atreya, S.K., 2004. Current state of modeling the photochemistry of Titan's mutually dependent atmosphere and ionosphere. J. Geophys. Res. 109, E06002.

Yelle, R.V., Borggren, N., de la Haye, V., Kasprzak, W.T., Niemann, H.B., Mueller-Wodarg, I., Waite Jr., J.H., 2006. The vertical structure of Titan's upper atmosphere from Cassini Ion Neutral Mass Spectrometer measurements. Icarus 182, 567–576.

Yelle, R.V., Cui, J., Mueller-Wodarg, I.C.F., 2008. Eddy diffusion and methane escape from Titan's atmosphere. J. Geophys. Res. 113, E10003. http://dx.doi.org/10.1029/2007JE003031.

Yung, Y.L., Allen, M., Pinto, J.P., 1984. Photochemistry of the atmosphere of Titan: Comparison between model and observations. Astrophys. J. Suppl. Ser. 55, 465–506.